

# High-resolution photoelectron spectroscopy of the pyridinide isomers

Cite as: J. Chem. Phys. 151, 064302 (2019); <https://doi.org/10.1063/1.5115413>

Submitted: 17 June 2019 . Accepted: 10 July 2019 . Published Online: 08 August 2019

Jessalyn A. DeVine , Mark C. Babin , Katherine Blackford, and Daniel M. Neumark 



View Online



Export Citation



CrossMark

The Journal  
of Chemical Physics

Submit Today

The Emerging Investigators Special Collection and Awards  
Recognizing the excellent work of early career researchers!



# High-resolution photoelectron spectroscopy of the pyridinide isomers

Cite as: J. Chem. Phys. 151, 064302 (2019); doi: 10.1063/1.5115413

Submitted: 17 June 2019 • Accepted: 10 July 2019 •

Published Online: 8 August 2019



View Online



Export Citation



CrossMark

Jessalyn A. DeVine,  Mark C. Babin,  Katherine Blackford, and Daniel M. Neumark<sup>a)</sup> 

## AFFILIATIONS

Department of Chemistry, University of California, Berkeley, California 94720, USA and Chemical Sciences Division, Lawrence Berkeley National Laboratory, Berkeley, California 94720, USA

<sup>a)</sup> Author to whom correspondence should be addressed: [dneumark@berkeley.edu](mailto:dneumark@berkeley.edu)

## ABSTRACT

Isomer-specific, high-resolution photoelectron spectra of cryogenically cooled pyridinide anions obtained using slow photoelectron velocity-map imaging are presented. New vibrational structure in the detachment spectrum of *para*-pyridinide is resolved, and the spectra of *meta*- and *ortho*-pyridinide are reported for the first time. These spectra yield electron affinities of 1.4797(5), 1.4473(5), and 0.8669(7) eV for the *para*-, *meta*-, and *ortho*-pyridyl radicals, respectively, as well as a number of vibrational frequencies for each neutral isomer. While most of the resolved structure in all three spectra is readily assigned by comparison to B3LYP/6-311+G\* Franck-Condon simulations, the *para*-pyridinide spectrum shows newly resolved fine structure attributed to anharmonic coupling within the vibrational manifold of the corresponding neutral radical. Isomeric trends in the photoelectron angular distributions are rationalized by approximating the detached anion orbitals as superpositions of *s*-, *p*-, and *d*-like hydrogenic orbitals, based on an application of Sanov's generalized mixing model [D. Khuseynov *et al.*, J. Chem. Phys. **141**, 124312 (2014)]. The presented experimental and theoretical results are used to address the relative energies of the anion and neutral isomers, as well as the site-specific bond dissociation energies of pyridine.

Published under license by AIP Publishing. <https://doi.org/10.1063/1.5115413>

## I. INTRODUCTION

Nitrogen-containing aromatic heterocycles such as pyridine (C<sub>5</sub>H<sub>5</sub>N) are common building blocks of coal and other high energy density materials.<sup>1–4</sup> Combustion of these species contributes to atmospheric NO<sub>x</sub> formation;<sup>5</sup> thus, studies of the thermal decomposition of pyridine are important for understanding the environmental impact of such fuels.<sup>6</sup> The chemistry of pyridine and its derivatives are also of interest to astronomers, particularly following the observation of nitrogen-containing compounds in the atmosphere of Titan.<sup>7,8</sup> Mechanistic studies of the thermal decomposition of pyridine have established that the first step is hydrogen loss resulting in formation of the *o*-, *m*-, or *p*-pyridyl radical, shown in Fig. 1.<sup>9–13</sup> Due to the prevalence of pyridine and the products of its decomposition in a wide range of chemical environments, spectroscopic characterization of the pyridyl radicals is of considerable interest. In this work, high-resolution anion photoelectron spectroscopy (PES) of cryogenically cooled pyridinide anions is used to obtain

isomer-specific spectra that reflect the vibronic structure of the neutral pyridyl radicals, providing quantitative and qualitative insight into these species.

Pyridyl radicals have been characterized using several methods aimed at understanding their inherent molecular properties as well as their reactivity and thermochemistry.<sup>14–17</sup> The H-loss channels that result from ultraviolet photodissociation of *m*- and *o*-pyridyl have been observed by Lucas and co-workers,<sup>18,19</sup> who used photolysis of 3- and 2-bromopyridine to generate the desired radical isomers. Korte *et al.*<sup>20</sup> used a similar method based on photolytic cleavage of a halogen-carbon bond to obtain a matrix infrared spectrum of the products, reporting several weak vibrational signatures attributed to the pyridyl radicals. Electron spin resonance spectroscopy, which is specifically sensitive to radical species, has been used to observe the pyridyl radicals in inert matrices<sup>21–23</sup> and in aqueous solution.<sup>24</sup>

Whereas free radicals are typically highly reactive species that can be difficult to isolate in a laboratory experiment,

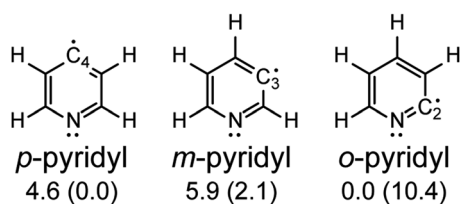


FIG. 1. The three isomeric forms of the pyridyl radical. Zero corrected B3LYP/6-311+G\* relative energies of the neutral (anion) isomers are provided in units of kcal mol<sup>-1</sup>.

the corresponding closed-shell anions are relatively long-lived in the gas phase and can readily be mass-selected prior to spectroscopic investigation. Thus, a versatile approach to characterization of neutral radicals is anion photoelectron spectroscopy (PES) of mass-selected anions.<sup>25</sup> PES of molecular anions simultaneously probes the electronic and vibrational structure of the corresponding neutrals, provided the spectral resolution is sufficient, and the photoelectron angular dependence can provide insight into the molecular orbital on the anion from which the electron is detached.<sup>26</sup> This strategy has been used previously by several groups to obtain spectroscopic access to the  $p$ -pyridyl radical by photodetachment of the  $p$ -pyridinide anion.<sup>27–29</sup> In all of these studies, pyridinide anions were generated by gas phase deprotonation of pyridine, so only the  $p$ -pyridinide isomer was formed owing to the observed regioselectivity of this process.<sup>30</sup>

To date, the highest-resolution photoelectron spectrum of the  $p$ -pyridinide anion is that reported by Wren and co-workers,<sup>27</sup> who observed an isolated vibrational origin with 11 meV full-width at half-maximum (FWHM) followed by increasingly complex and partially resolved vibrational structure. This work provided an electron affinity (EA) of 1.480(6) eV as well as two vibrational frequencies ( $600 \pm 20$  and  $1010 \pm 50$  cm<sup>-1</sup>) for the  $p$ -pyridyl radical. With experimental gas phase acidity measurements, this EA was used to obtain a bond dissociation enthalpy (BDE) of  $110.4 \pm 2.0$  kcal mol<sup>-1</sup> for the C<sub>4</sub>H bond (see Fig. 1) of pyridine. Subsequent work using photoelectron imaging of the  $p$ -pyridinide anion was reported by Culberson and co-workers.<sup>28</sup> This spectrum did not show any vibrational structure, but the photoelectron angular distribution (PAD) was used as a test case for the mixed- $sp$  model developed by Sanov,<sup>31</sup> which provides an intuitive framework for understanding how experimental PADs are related to the hybridization of anion orbitals. This model has been successfully used to assess the PADs for detachment from a number of organic anions.<sup>29,32,33</sup>

Slow electron velocity-map imaging (SEVI) is a variant of traditional anion PES wherein a velocity-map imaging (VMI) detection scheme and a tunable detachment laser are combined to obtain narrow windows of the photoelectron spectrum with submillielectron volt resolution, which are then concatenated to give a full high-resolution spectrum.<sup>34,35</sup> By cooling ions to internal temperatures of  $\sim 10$  K prior to detachment (cryo-SEVI), rotational broadening and spectral congestion are minimized, yielding transitions as narrow as 1.2 cm<sup>-1</sup> FWHM that reflect the vibronic structure of the

corresponding neutral.<sup>36,37</sup> Cryo-SEVI has been highly successful in revealing subtleties in the vibronic structure of a number of aromatic radicals;<sup>32,38–41</sup> in cases where multiple radical isomers are possible, reaction of appropriate trimethylsilyl (TMS) substituted precursors with fluoride anions has enabled acquisition of isomer-specific spectra.<sup>32,40,41</sup>

Here, we use this approach to obtain cryo-SEVI spectra for the three anion isomers of deprotonated pyridine. These results represent the first reported photoelectron spectra of the  $m$ - and  $o$ -pyridinide anions and provide a substantial improvement in resolution for the  $p$ -pyridinide detachment spectrum. Comparison of the spectra to B3LYP/6-311+G\* calculations enables extraction of multiple vibrational frequencies and EAs for all three radical isomers. While the majority of features in all three spectra are well-described by harmonic Franck-Condon (FC) simulations, anharmonic mixing between vibrational levels of the  $p$ -pyridyl radical is proposed as the cause of  $\sim 10$  cm<sup>-1</sup> experimental peak splittings observed for several detachment transitions from the corresponding anion isomer. To describe the photoelectron angular distributions for all three anions in a unified framework, the mixed- $sp$  model has been expanded to include a  $d$ -component following the generalized mixing model developed by Sanov,<sup>42</sup> and the results of this treatment highlight isomeric trends in orbital hybridization for deprotonated pyridine. Finally, the experimental and theoretical results presented here are used to consider the origin of the relative isomeric stabilities for both charge states, and estimates of the CH BDEs of pyridine are obtained using a combined experimental-theoretical approach.

## II. EXPERIMENTAL METHODS

The cryo-SEVI method has been described in detail previously.<sup>34,36,41</sup> To generate pyridinide anions, a gas mixture consisting of trace NF<sub>3</sub> in He is passed over a temperature-controlled cartridge containing a molecular precursor. The precursor is entrained in the carrier gas, which then undergoes supersonic expansion through an Even-Lavie valve fitted with a circular filament ionizer.<sup>43</sup> Injection of electrons from the ionizer into the gas expansion results in dissociative electron attachment to NF<sub>3</sub> forming fluoride anions, which react with the molecular precursor to produce the ion of interest.

The use of pyridine as the molecular precursor resulted in formation of both  $m$ - and  $p$ -pyridinide, as shown in Fig. S1 of the [supplementary material](#). To obtain isomer-specific spectra, the valve cartridge was loaded with the appropriate isomer of trimethylsilyl(TMS)pyridine, which then reacted with F<sup>-</sup> in the pulsed gas expansion to produce the desired anion isomer and TMS fluoride.<sup>44,45</sup> 2-(TMS)pyridine was purchased from Sigma Aldrich and used as the precursor for generation of  $o$ -pyridinide. The precursors for  $m$ - and  $p$ -pyridinide were synthesized as described in Sec. S1 of the [supplementary material](#). To prevent isomerization of the 4-(TMS)pyridine precursor, the Even-Lavie valve body was held at a temperature of 25 °C.

After supersonic expansion, ions pass through a radiofrequency (RF) hexapole ion guide and quadrupole mass filter and are injected into a RF octupole ion trap.<sup>36</sup> The trap is cooled to  $\sim 5$  K by a closed-cycle helium compressor and filled with  $\sim 10^{-3}$  Torr of a buffer gas mixture consisting of 20% H<sub>2</sub> in He. While stored in the trap, ions

undergo  $\sim 10^3$ – $10^4$  collisions with the cold buffer gas molecules, resulting in efficient relaxation of rovibrationally and/or electronically excited states to ensure that the detachment spectra are free of hot bands and to reduce spectral broadening from unresolved rotational transitions. Typical ion temperatures are estimated to be  $\sim 10$  K at the point of photodetachment using this cooling scheme.

After  $\sim 40$  ms in the trap, ions are extracted into an orthogonal Wiley-McLaren time-of-flight mass spectrometer<sup>46</sup> and focused into the interaction region of a velocity-map imaging (VMI) spectrometer,<sup>41,47</sup> where the ions of interest are photodetached by a tunable laser. The VMI spectrometer is optimized for the collection of slow photoelectrons, as described previously.<sup>34,41</sup> Two different laser configurations were required to obtain the spectra reported in the current work. For the *p*- and *m*-pyridinide anions, the spectra were obtained using the output of a tunable dye laser pumped by the second harmonic of an Nd:YAG laser. Due to the lower electron affinity of the *o*-pyridyl isomer, a Raman shifter cell containing 380 psi of H<sub>2</sub><sup>48</sup> was used to obtain the photon energies necessary to obtain a high-resolution spectrum for this isomer.

The detached electrons are projected onto a position-sensitive detector comprising two chevron-stacked microchannel plates coupled to a phosphor screen, the back of which is photographed by a CCD camera after each laser shot.<sup>49</sup> These images are analyzed in real-time for individual electron events, the centroids of which are calculated and binned in a grid sufficiently large to ensure that spectral resolution is not limited by pixel size.<sup>50</sup> The 3D electron velocity distribution is reconstructed using the maximum entropy velocity Legendre reconstruction (MEVELER) method, generating a reconstructed image which represents a vertical slice through the diameter of the three-dimensional electron velocity distribution.<sup>51</sup> The radial positions of features in the reconstructed images are related to electron kinetic energy (eKE) by acquisition of images for the well-characterized detachment transitions of Ni<sup>-</sup> and O<sup>-</sup> at several photon energies.<sup>52,53</sup> Spectra are plotted vs electron binding energy (eBE), given by  $eBE = h\nu - eKE$ .

Due to the roughly constant resolving power,  $\Delta eKE/eKE$ , of the VMI spectrometer, the best resolution is obtained for low-eKE photoelectrons. As such, a cryo-SEVI spectrum is constructed by first acquiring an overview scan taken far from threshold, where the relative intensities of different features are less strongly impacted by near-threshold scaling of the detachment cross section. For each feature of interest in the overview spectrum, a high-resolution scan is then obtained by tuning the detachment laser to within  $\sim 100$  cm<sup>-1</sup> of the observed eBE, giving narrow windows of the spectrum in high resolution. For detachment from atomic anions, this yields features as narrow as 1.2 cm<sup>-1</sup> FWHM; typical peak widths observed in the high-resolution spectra of the current work are on the order of 10 cm<sup>-1</sup> FWHM.

The VMI technique enables simultaneous measurement of the photoelectron angular distribution (PAD) for each detachment transition, given by<sup>54</sup>

$$\frac{d\sigma}{d\Omega} = \frac{\sigma_{tot}}{4\pi} [1 + \beta P_2(\cos\theta)], \quad (1)$$

where  $\sigma_{tot}$  is the total detachment cross section for the transition of interest,  $P_2(x)$  is the second-order Legendre polynomial,  $\theta$  is

the angle of the outgoing electron's velocity vector with respect to the laser polarization axis, and  $\beta$  is the anisotropy parameter. The anisotropy parameter ranges from  $-1$  to  $+2$  corresponding to perpendicular and parallel detachment, respectively, and its variation as a function of eKE reflects the symmetry and angular momentum properties of the anion orbital from which an electron is removed.<sup>26</sup>

### III. COMPUTATIONAL METHODS

With the exception of the thermochemical calculations detailed below, all computations were carried out at the B3LYP/6-311+G\* level using QChem version 5.1.<sup>55</sup> Geometry optimizations for all three anion and neutral isomers were performed giving the results provided in Tables S1–S3 of the [supplementary material](#). Harmonic frequency calculations were also performed for all six species, and the resulting frequencies for all anion and neutral isomers are provided in Table S4.

The B3LYP/6-311+G\* geometries, harmonic frequencies, and normal mode displacements were used as input for the ezSpectrum software package,<sup>56</sup> which calculates the Franck-Condon (FC) factors for detachment from the anion ground state to various vibrational levels of the neutral, including Duschinsky mixing to account for differences between anion and neutral normal modes. To provide a better match with experimental frequencies, the shifts from the origin were scaled by 0.975, 0.977, and 0.979 in the *p*-, *m*-, and *o*-pyridinide FC simulations, respectively. To further improve agreement with experiment for the *o*-pyridinide spectrum, small displacements along the  $\nu_5$  mode were applied to the B3LYP/6-311+G\* equilibrium geometry of *o*-pyridyl used to calculate the FC profile for this isomer, as described in Sec. V A. A comparison of the B3LYP/6-311+G\* equilibrium and shifted FC profiles is presented in Fig. S2 of the [supplementary material](#), and the neutral geometry used for the FC simulation which best matches experiment is summarized in Table S5.

To estimate gas-phase acidities for the three deprotonation sites of pyridine, thermochemical calculations were carried out using Gaussian 16.<sup>57</sup> Absolute enthalpies of pyridine and the three pyridinide anions at  $T = 298.15$  K, as well as those of the neutral radicals, were calculated using the CBS-QB3 method.<sup>58,59</sup> Experimental-theoretical gas-phase acidities for the C<sub>3</sub> and C<sub>2</sub> positions are calculated using the experimental  $\Delta H_{acid}^{\circ}$  of the C<sub>4</sub> position, which is the only position for which an experimental measurement of this quantity is available. With the differences in absolute enthalpies defined as

$$\delta_n = H^{298}(n\text{-pyridinide}) - H^{298}(4\text{-pyridinide}), \quad (2)$$

the acidities of the two carbon positions, for which there are no experimental measurements of  $\Delta H_{acid}^{\circ}$ , are approximated as  $\Delta H_{acid}^{\circ}(C_n) = \delta_n + \Delta H_{acid}^{\circ}(C_4)$ . The calculated absolute enthalpies for all three anion and neutral isomers, as well as pyridine, are provided in Table S6 of the [supplementary material](#).

### IV. RESULTS

The TMS-substituted molecular precursors used for anion generation enable acquisition of isomer-specific cryo-SEVI spectra of *p*-, *m*-, and *o*-pyridinide, shown in Figs. 2–4. In all cases, blue traces represent overview scans taken at relatively high photon

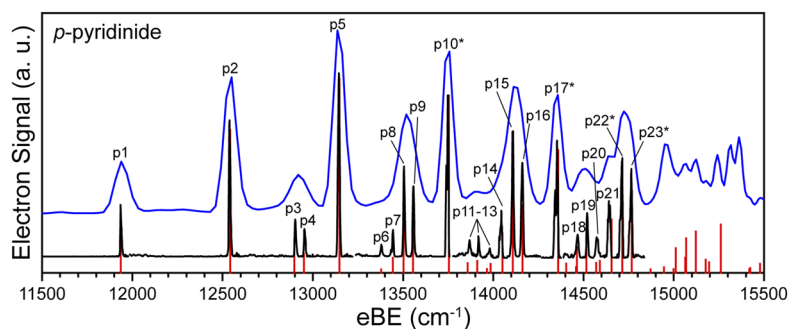


**FIG. 2.** Cryo-SEVI spectrum of *p*-pyridinide. The blue trace corresponds to an overview spectrum taken with a photon energy of 15873  $\text{cm}^{-1}$ , and the black traces are high-resolution scans taken near threshold. A Franck-Condon simulation based on B3LYP/6-311+G\* results is shown as red sticks, where shifts from the origin have been scaled by a factor of 0.975.

energies, and black traces are low-eKE, high-resolution scans taken closer to threshold. The red stick spectra show the Franck-Condon simulations used for vibrational assignments and will be discussed in more detail in Sec. V.

The cryo-SEVI spectrum of *p*-pyridinide (Fig. 2) exhibits a number of well-resolved transitions (p1–p23) with typical peak widths of 8–10  $\text{cm}^{-1}$  FWHM. The binding energies of these features are summarized in Table S7 of the [supplementary material](#). The spectrum in Fig. 2 represents a substantial improvement over prior results, and the lowest eBE peak at p1 gives an EA of 1.4797(5) eV for the *p*-pyridyl radical. The vibrational progressions reported by Wren and co-workers<sup>27</sup> are observed here in higher resolution, giving refined frequencies of 603(5)  $\text{cm}^{-1}$  (p1–p2–p10–p17) and 1020(6)  $\text{cm}^{-1}$  (p1–p4, p2–p9, etc.). In addition to these previously resolved progressions, new underlying vibrational structure is observed. As shown in Fig. 5, high-resolution scans taken close to

threshold show that feature p10 is a doublet of peaks (p10a/b) split by 9  $\text{cm}^{-1}$ . Similar splittings are found for peaks p17, p22, and p23.

The cryo-SEVI spectrum of *m*-pyridinide (Fig. 3) represents the first reported PE spectrum for this anion isomer and shows vibrational structure similar to that observed for the *para* isomer. Features in the m1–m28 series (Table S8 of the [supplementary material](#)) have typical peak widths of 9–11  $\text{cm}^{-1}$  FWHM. The first peak occurs at a slightly lower eBE than is seen in the *p*-pyridinide spectrum, giving an EA of 1.4473(5) eV for the *m*-pyridyl radical. The vibrational structure in this spectrum shows a dominant progression (m1–m3–m8–m16–m25) with  $\sim 650 \text{ cm}^{-1}$  splitting, and the remaining intense features observed in the overview spectrum (m4, m11, m21) correspond to a modulation of this progression by a mode with frequency 974(6)  $\text{cm}^{-1}$ . In addition, the high-resolution traces show a number of weak transitions that are obscured by more intense features in the overview spectrum.

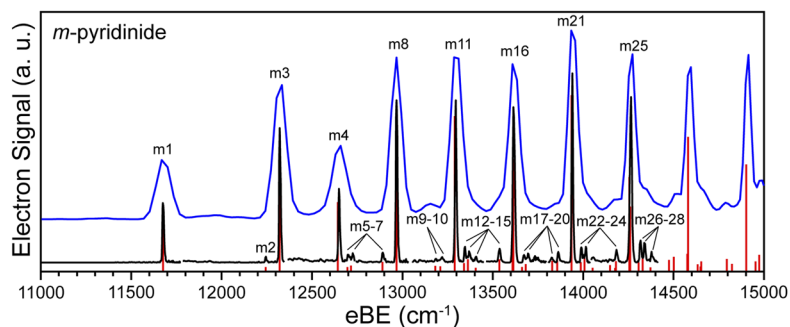


**FIG. 3.** Cryo-SEVI spectrum of *m*-pyridinide. The blue trace corresponds to an overview spectrum taken with a photon energy of 15873  $\text{cm}^{-1}$ , and the black traces are high-resolution scans taken near threshold. A Franck-Condon simulation based on B3LYP/6-311+G\* results is shown as red sticks, where shifts from the origin have been scaled by a factor of 0.977.

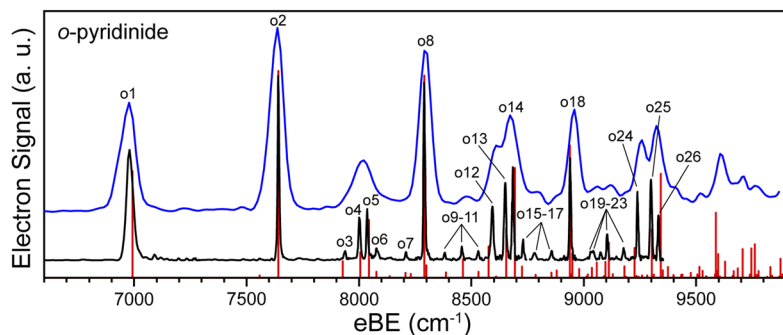


**FIG. 4.** Cryo-SEVI spectrum of *o*-pyridinide. The blue trace corresponds to an overview spectrum taken with a photon energy of 11300  $\text{cm}^{-1}$ , and the black traces are high-resolution scans taken near threshold. The Franck-Condon simulation based on the shifted neutral geometry is shown as a red stick spectrum, where the neutral frequencies have been scaled by a factor of 0.979.

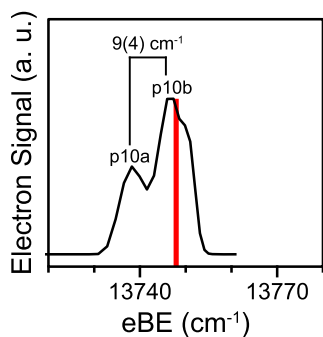


**FIG. 5.** High-resolution scan showing the splitting of feature p10 in the cryo-SEVI spectrum of *p*-pyridinide. The red stick shows the  $9_0^3$  transition of the *p*-pyridinide B3LYP/6-311+G\* FC simulation.

The cryo-SEVI spectrum of the *o*-pyridinide isomer, shown in Fig. 4, comprises a number of features (o1–o25) with similar resolution to that obtained for the other two anion isomers. The peak positions and widths are summarized in Table S9 of the supplementary material. As is the case for the other isomers, the cryo-SEVI spectrum of *o*-pyridinide is dominated by a single progression (o1–o2–o8–o18), which is modulated by several less intense patterns. This dominant progression gives a harmonic frequency of  $649(5) \text{ cm}^{-1}$  for the *o*-pyridyl radical. In addition, a closely spaced doublet of peaks split by  $10 \text{ cm}^{-1}$ , o19/o20, is resolved. This splitting may be seen more clearly in Fig. S3 of the supplementary material.

The laser scheme used to obtain the high-resolution spectra of the *o*-pyridinide anion involves a single-pass Raman shifter cell, which extends the tuning range of the dye laser system to photon energies as low as  $\sim 7300 \text{ cm}^{-1}$ .<sup>48</sup> This is still several hundred  $\text{cm}^{-1}$  above the photon energies that would be required to obtain optimal resolution for the vibrational origin (o1), and as a result, this feature has a larger reported width ( $30 \text{ cm}^{-1}$  FWHM) than the higher-eBE features o2–o26 ( $7\text{--}10 \text{ cm}^{-1}$  FWHM). Thus, rather than using feature o1 to extract the electron affinity of the neutral radical, we take the EA to be given by the eBE of the first feature in the dominant progression (o2) minus the harmonic frequency of  $649(5) \text{ cm}^{-1}$  extracted from the dominant progression, giving a final EA of  $0.8669(7) \text{ eV}$  for the *o*-pyridyl radical. This value of the EA is used to calculate the shifts of features o2–o26 given in Table S9.

## V. DISCUSSION

### A. Vibrational assignments

#### 1. *p*-pyridinide

The cryo-SEVI spectrum of *p*-pyridinide (Fig. 2) shows excellent agreement with the B3LYP/6-311+G\* Franck-Condon simulation, providing vibrational assignments for the majority of observed features as transitions terminating in FC-allowed vibrational levels of *p*-pyridyl. These assignments are presented in Table S7 of the supplementary material. The dominant

progression (p1–p2–p10–p17) is assigned to the  $\nu_9$  mode, a ring distortion mode which heavily involves the radical-centered  $\text{C}_3\text{--C}_4\text{--C}_3$  angle (see Fig. S4 of the supplementary material). The high degree of FC activity for this mode arises from the relatively large change in this geometrical parameter, which increases from  $110.2^\circ$  to  $124.0^\circ$  between the anion and neutral equilibrium geometries. Four other vibrational frequencies are extracted based on the positions of the corresponding vibrational fundamentals relative to the vibrational origin (p3–p7). These frequencies are summarized in Table I, where they are compared to the calculated B3LYP/6-311+G\* harmonic values.

The high-resolution scan for feature p10 (Fig. 5) reveals that this peak in fact consists of two separate transitions (p10a/b), while only a single transition ( $9_0^3$ ) is predicted in the FC simulation. Similar splittings are observed for features p17, p22, and p23. Given the relatively small magnitude of the observed splitting, one possible source of these unexplained features is a Fermi resonance between the  $3\nu_9$  level (which plays a role in all FC transitions showing the  $\sim 10 \text{ cm}^{-1}$  splitting) and some other totally symmetric vibrational level. This level would then gain its observed FC-activity through anharmonic mixing with the  $3\nu_9$  level. Coupling of this nature is particularly likely for levels that are close in energy, such as the Fermi resonance between the  $1\nu_{39}$  and  $1\nu_{59} + 1\nu_{61}$  vibrational levels of the 1-anthracenyl radical, which was found to result in the appearance of the  $59_0^1 61_0^1$  detachment transition in the cryo-SEVI spectrum of the 1-anthracenyl anion.<sup>41</sup> In that case, the totally symmetric  $1\nu_{39}$  vibrational state interacts with a totally symmetric combination band of nontotally symmetric modes, resulting in an  $8 \text{ cm}^{-1}$  splitting in the  $\nu_{39}$  fundamental (as well as FC-predicted combination bands involving this mode).

Consideration of the B3LYP harmonic frequencies of the *p*-pyridyl radical (Table S4 of the supplementary material) shows that the closest totally symmetric combination band which could give rise to the  $10 \text{ cm}^{-1}$  splitting is the  $1\nu_8 + 2\nu_{16}$  level, whose calculated harmonic energy is  $9 \text{ cm}^{-1}$  higher than that of  $3\nu_9$ . Thus, we tentatively assign the state which interacts with  $3\nu_9$  to give rise to the splitting observed for features p10a/b (p17a/b, p22a/b, p23a/b) to the  $8_0^1 16_0^2$  ( $8_0^1 9_0^1 16_0^2$ ,  $8_0^2 16_0^2$ ,  $7_0^1 8_0^1 16_0^2$ ) transition. As each pair of states is strongly coupled, the neutral levels accessed in each transition likely correspond to an admixture of the two vibrational levels. Keeping this in mind, we may treat the  $\nu_9$  progression as an anharmonic series [Sec. S2 and Eq. (S1)], and this shows that p10b is most appropriate to assign as the FC-allowed  $9_0^3$  detachment

**TABLE I.** Molecular parameters of the *p*-pyridyl radical obtained from the cryo-SEVI spectra of the corresponding anion. Theoretical values obtained from a harmonic B3LYP/6-311+G\* analysis are also provided.

	SEVI	B3LYP
EA (eV)	1.4797(5)	1.4725
$\nu_3$ ( $\text{cm}^{-1}$ )	1509(4)	1543
$\nu_4$ ( $\text{cm}^{-1}$ )	1445(5)	1476
$\nu_7$ ( $\text{cm}^{-1}$ )	1020(6)	1038
$\nu_8$ ( $\text{cm}^{-1}$ )	969(6)	983
$\nu_9$ ( $\text{cm}^{-1}$ )	603(5)	620

transition; similarly, p17b, p22b, and p23b are assigned to the FC-allowed  $9_0^4$ ,  $8_0^1 9_0^3$ , and  $7_0^1 9_0^3$  transitions, respectively, suggesting that peaks p10a, p17a, p22a, and p23a are best described as the  $8_0^1 16_0^2$ ,  $8_0^1 9_0^1 16_0^2$ ,  $8_0^2 16_0^2$ , and  $7_0^1 8_0^1 16_0^2$  transitions, respectively. However, as noted above, this is only one possible explanation for the observed splitting.

## 2. *m*-pyridinide

The B3LYP/6-311+G\* FC simulation for detachment from *m*-pyridinide, shown as red sticks in Fig. 3, accounts for all observed transitions in the cryo-SEVI spectrum for this isomer, allowing for assignment of peaks m1–m28 as detachment transitions terminating in totally symmetric vibrational levels of the *m*-pyridyl radical. These assignments are provided in Table S8 of the [supplementary material](#). The dominant progression (m1–m3–m8–m16–m25) is attributed to the  $\nu_{16}$  vibrational mode, a ring distortion that involves the C<sub>4</sub>–C<sub>3</sub>–C<sub>2</sub> bond angle centered on the deprotonated carbon atom. The second-most FC active mode which modulates the  $\nu_{16}$  progression (m4, m11, m21) is identified as  $\nu_{17}$ , another ring-distortion mode that involves the C<sub>2</sub>–N–C<sub>2</sub> and C<sub>3</sub>–C<sub>4</sub>–C<sub>3</sub> angles.

A total of 7 vibrational modes of *m*-pyridyl play a role in the spectrum; these are pictured in Fig. S5 of the [supplementary material](#), and their experimental frequencies are reported in Table II. Several of the measured frequencies have been identified previously in the matrix-IR study of the products formed by photolysis of 3-iodopyridine,<sup>20</sup> and the reported IR frequencies are included in Table II. As was the case for the *para* isomer, the strong involvement of ring-distortion modes involving the C<sub>4</sub>–C<sub>3</sub>–C<sub>2</sub> angle centered on the radical carbon can be attributed to the difference in equilibrium values between anion and neutral (110.8° and 123.8°, respectively).

## 3. *o*-pyridinide

The experimental cryo-SEVI spectrum of *o*-pyridinide shows excellent agreement with the Franck-Condon simulation in Fig. 4, enabling assignment of all resolved features (Table S9). The dominant progression (o1–o2–o8–o18) is assigned to the  $\nu_{16}$  mode, an in-plane ring distortion which involves bending of the C<sub>2</sub>–N–C<sub>2</sub> angle as well as stretching of the C<sub>2</sub>–C<sub>3</sub> bonds (Fig. S6). Other vibrational

**TABLE II.** Molecular parameters of the *m*-pyridyl radical obtained from the cryo-SEVI spectra of the corresponding anion. Theoretical values obtained from a harmonic B3LYP/6-311+G\* analysis are also provided, as are available vibrational frequencies observed previously in an Ar matrix.

	SEVI	B3LYP	Matrix IR <sup>20</sup>
EA (eV)	1.4473(5)	1.4391	
$\nu_6$ (cm <sup>-1</sup> )	1509(6)	1543	1499.9
$\nu_{12}$ (cm <sup>-1</sup> )	1085(6)	1110	1084.9
$\nu_{13}$ (cm <sup>-1</sup> )	1050(8)	1065	1035.9
$\nu_{14}$ (cm <sup>-1</sup> )	1027(8)	1044	
$\nu_{15}$ (cm <sup>-1</sup> )	974(6)	990	
$\nu_{16}$ (cm <sup>-1</sup> )	646(6)	662	646.3
$\nu_{17}$ (cm <sup>-1</sup> )	568(5)	581	569.5

fundamentals (o3–o6, o9–o11) are also observed; while the eBEs of these fundamentals would typically be used to extract vibrational frequencies by calculating their shifts relative to the vibrational origin (o1), we have instead used the  $16_0^1$  (o2) and  $x_0^1 16_0^1$  (o7, o12, o13, o14, o15, o16, o19, o22, and o23) peaks to obtain the vibrational frequencies  $\nu_x$  presented in Table III due to the narrower peak width obtained for feature o2 relative to o1. Ten vibrational frequencies for the *o*-pyridyl radical are extracted in this manner, with uncertainties ranging from 4 to 7 cm<sup>-1</sup>. Two of these frequencies,  $\nu_{13} = 1043(5)$  cm<sup>-1</sup> and  $\nu_{17} = 568(5)$  cm<sup>-1</sup>, were previously assigned in the matrix isolation study of Korte and co-workers,<sup>20</sup> who gave frequencies of 1044 and 565 cm<sup>-1</sup>, respectively.

The FC simulation based on the B3LYP/6-311+G\* equilibrium geometries (Fig. S2a) predicts that a relatively intense feature, corresponding to the  $5_0^1$  transition, should appear between features o12 ( $15_0^1 16_0^1$ ) and o13 ( $14_0^1 16_0^1$ ). This feature was not observed in the experimental spectrum. Such a discrepancy can result from slight inaccuracies in the calculated anion/neutral geometries, which then leads to overestimation or underestimation of the displacement along particular vibrational modes corresponding to anomalously high or low FC intensities. To investigate this possibility in the *o*-pyridinide detachment spectrum, a number of FC simulations were performed for detachment from the B3LYP/6-311+G\* equilibrium anion geometry to a neutral geometry defined by  $\bar{r}^{(i)} = \bar{r}_{eq}^{(i)} + \xi \bar{q}_5^{(i)}$ , where  $\bar{r}_{eq}^{(i)}$  is the B3LYP/6-311+G\* equilibrium position of atom *i*,  $\bar{q}_5^{(i)}$  is the atomic displacement vector for atom *i* associated with  $\nu_5$ , and  $\xi$  defines the magnitude of the shift. This parameter was varied to yield shifted neutral geometries, which were then used to calculate the Franck-Condon profile for detachment from the equilibrium anion geometry. This enabled determination of the magnitude of shift  $\xi$  necessary to account for the absence of the  $5_0^1$  transition in the experimental spectrum.

As shown in Fig. S2 of the [supplementary material](#), the FC intensity of this transition is approximately quadratic in  $\xi$ , reaching a minimum at a shift of  $\xi = -0.0625$ . The corresponding root-mean-square change in the neutral geometry, defined by  $[\sum (\bar{r}^{(i)} - \bar{r}_{eq}^{(i)})^2]^{1/2}$ , is only 0.062 Å, with the most substantial

**TABLE III.** Molecular parameters of the *o*-pyridyl radical obtained from the cryo-SEVI spectra of the corresponding anion. Theoretical values obtained from a harmonic B3LYP/6-311+G\* analysis are also provided.

	SEVI	B3LYP
EA (eV)	0.8669(7)	0.8236
$\nu_6$ (cm <sup>-1</sup> )	1536(5)	1572
$\nu_7$ (cm <sup>-1</sup> )	1463(5)	1502
$\nu_8$ (cm <sup>-1</sup> )	1390(4)	1424
$\nu_{11}$ (cm <sup>-1</sup> )	1140(7)	1169
$\nu_{12}$ (cm <sup>-1</sup> )	1088(4)	1108
$\nu_{13}$ (cm <sup>-1</sup> )	1043(5)	1074
$\nu_{14}$ (cm <sup>-1</sup> )	1010(5)	1035
$\nu_{15}$ (cm <sup>-1</sup> )	951(6)	956
$\nu_{16}$ (cm <sup>-1</sup> )	649(5)	663
$\nu_{17}$ (cm <sup>-1</sup> )	568(5)	578

change corresponding to a 0.06 Å increase in the bond length between the nitrogen and the deprotonated carbon atom (see Table S5). Given the fairly small geometry adjustment required to bring the calculated intensity of the  $\nu_5$  fundamental to near-zero, we take the absence of the  $5_0^1$  transition in the cryo-SEVI spectrum to be a consequence of the true neutral geometry, which differs slightly from that predicted by B3LYP/6-311+G\* calculations. The  $\xi = -0.0625$  FC simulation is shown alongside the experimental results in Fig. 4, and a comparison of this simulation to that obtained using the neutral equilibrium B3LYP/6-311+G\* geometry is provided in Fig. S2.

## B. Photoelectron angular distributions

Figure 6 shows the eKE-dependence of the anisotropy parameters observed for detachment from the three pyridinide anions. It was found that for each isomer, all resolved features show similar anisotropies, indicating that each spectrum in Figs. 2–4 involves a single electronic transition. The PADs for the three isomers are clearly different; the *para* and *meta* isomers show perpendicular detachment ( $\beta < 0$ ), with the *para* isomer yielding slightly more negative values of  $\beta$ . The *ortho* isomer exhibits parallel detachment ( $\beta > 0$ ) at low-eKEs that tends toward near-zero anisotropies as eKE increases.

The measured PADs reflect the angular momentum composition of the outgoing electron, which in turn is related to the anion orbital from which detachment occurs. For the pyridinide anions, the relevant orbitals are taken to be the highest-occupied molecular orbitals (HOMOs) shown in Fig. 7. These orbitals show that as the site of deprotonation moves toward the heteroatom, the resultant anion HOMO becomes more delocalized, with more involvement of the heteroatom. In particular, the HOMO of the *ortho* isomer shows considerable electron density around the nitrogen atom, as well as distinct nodal structure along the C<sub>2</sub>–N bond. Given the clear distinctions between the observed PADs, we aim to develop a conceptual framework that can connect these isomeric trends.

The anisotropy parameter for detachment from an anion orbital with well-defined angular momentum  $l$  is described by the

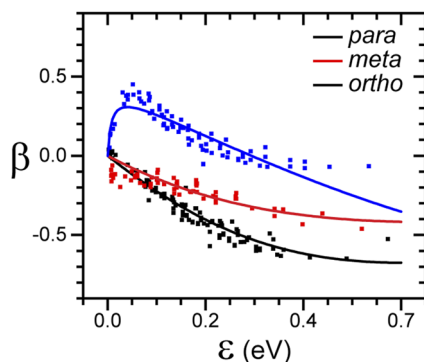


**FIG. 6.** Anisotropy parameters observed for photodetachment from *p*- (black), *m*- (red), and *o*-pyridinide (blue) as a function of electron kinetic energy. The solid lines show the results of fitting the experimental PADs to the mixed-*spd* model.

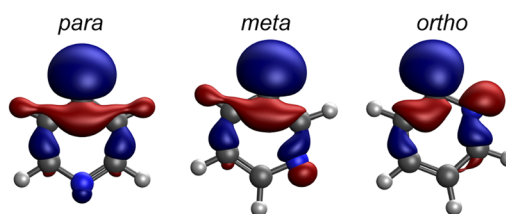


**FIG. 7.** Highest-occupied molecular orbitals of the three pyridinide anions as determined at the B3LYP/6-311+G\* level of theory.

Cooper-Zare equation [Eq. (S2)].<sup>54</sup> For  $l > 0$ , the outgoing electron is a superposition of  $l + 1$  and  $l - 1$  partial waves; at low eKEs, the relative scaling of these detachment channels is governed by the Wigner threshold law,<sup>60</sup> allowing for a direct expression of  $\beta$  as a function of eKE (Sec. S3a). For molecules,  $l$  is not a good quantum number, and such a single- $l$  treatment is unlikely to adequately describe observed angular distributions. Previously, the PAD for detachment from *p*-pyridinide has been modeled using the mixed-*sp* formulation of Sanov and co-workers (Sec. S3b),<sup>28,31</sup> where the detached anion orbital is assumed to be a combination of an  $s$  ( $|0\rangle$ ) and  $p$  ( $|1\rangle$ ) component with fractional  $p$ -character  $\gamma_1$ , i.e.,  $|\Psi_{MO}\rangle = \sqrt{1 - \gamma_1}|0\rangle + \sqrt{\gamma_1}|1\rangle$ . The basis functions are taken to be hydrogenic  $s$  and  $p$  orbitals [Eq. (S3)] defined by charge parameters  $Z_0$  and  $Z_1$ , which fully determine the Hanstorp coefficients  $A_1$  and  $B_1$  [Eq. (S4)] describing the relative scaling of different detachment channels in the Wigner limit.<sup>60,61</sup> Here,  $A_1$  describes the relative scaling between the  $p \rightarrow d$  and  $p \rightarrow s$  detachment channels, and  $B_1$  quantifies the relative scaling for the  $s \rightarrow p$  and  $p \rightarrow s$  channels.

With these assumptions, an explicit expression for the eKE( $\epsilon$ )-dependence of the anisotropy parameter may then be derived in terms of the fractional  $p$ -character  $\gamma_1$  as well as the  $A_1$  and  $B_1$  coefficients [Eq. (S5)]. For detachment from an orbital localized on a particular atomic center, the choice of  $A_1$  and  $B_1$  is fairly straightforward; in the previously reported treatment of *p*-pyridinide and other deprotonated aromatic anions,<sup>29</sup> the basis set parameterization was set to that typical for detachment from a  $2s$ - $2p$  orbital centered on a carbon atom,  $A_1 = 0.75 \text{ eV}^{-1}$  and  $B_1 = 8A_1/3$  (corresponding to  $Z_0 = Z_1 = 0.885$ ).<sup>62,63</sup> Using these, Eq. (S5) gives a single-parameter expression for  $\beta(\epsilon)$  that can be fit to experimental data to extract the fractional  $p$ -character of the detached orbital, giving a direct link between the experimental PAD and the orbital hybridization of the anion.<sup>29,32</sup>

The formulation of the mixed-*sp* model has since been expanded to a generalized mixing model,<sup>42</sup> described in Sec. S3c of the [supplementary material](#). In the generalized model, the detached MO is taken to be a linear combination of an arbitrary number of angular momentum components,  $|\Psi_{MO}\rangle = \sum_l \sqrt{\gamma_l}|l\rangle$ . This expansion of  $|\Psi_{MO}\rangle$  in terms of an atomic orbital basis set is valid for any orbital so long as it is centered about a particular point in space; thus, while these mixing models have typically been applied to orbitals which are primarily localized on a particular atom, a more delocalized orbital may also be treated so long as it is reasonably described by a single-center function. The resulting expression for the anisotropy parameter is given in Eq. (S6).

For *p*-pyridinide, the C-centered  $2s$ - $2p$  model is a logical choice for treating the anion HOMO, and the strong resemblance between the *m*- and *p*-pyridinide orbitals suggests that this is also an appropriate starting point for describing the *meta* isomer. However, the *o*-pyridinide HOMO (Fig. 7) is better described as being centered along the C<sub>2</sub>-N bond, and this picture suggests that appreciable *d*-character should be accounted for in an adequate treatment of this isomer. Thus, to understand the PADs of all three pyridinide isomers within a single conceptual framework, we have developed a mixed-*spd* model for photoelectron angular distributions as determined by Sanov's general formula.

The mixed-*spd* basis set consists of the same  $2s$  and  $2p$  hydrogenic orbitals (parameterized by  $Z_0$  and  $Z_1$ ) as well as a  $3d$  function [Eq. (S7), with charge parameter  $Z_2$ ] so that

$$|\Psi_{spd}\rangle = \sqrt{1-\gamma_1-\gamma_2}|0\rangle + \sqrt{\gamma_1}|1\rangle + \sqrt{\gamma_2}|2\rangle. \quad (3)$$

As described in Sec. S3d of the [supplementary material](#), the introduction of an  $l = 2$  contribution to the molecular orbital results in two new Hanstorp coefficients,  $A_2$  and  $B_2$ , which are fully determined by the basis set parameterization in a similar manner as  $A_1$  and  $B_1$  [Eq. (S8)]. Here,  $A_2$  gives the relative scaling of the cross sections for the  $d \rightarrow f$  and  $d \rightarrow p$  detachment channels, and  $B_2$  similarly quantifies the relationship between the  $p \rightarrow d$  and  $d \rightarrow p$  channels. In terms of the *p*- and *d*-characters of the anion MO ( $\gamma_1$  and  $\gamma_2$ , respectively), as well as the four Hanstorp coefficients, the mixed-*spd* application of the general model in Eq. (S6) can be shown to reduce to

$$\beta_{spd}(\varepsilon) = \frac{2\left[\frac{B_1}{A_1}(1-\gamma_1-\gamma_2) - 2\gamma_1 + \frac{1}{5}\frac{A_1}{B_2}\gamma_2\right]A_2\varepsilon + 2\left(\gamma_1 - \frac{18}{5}\frac{A_2}{B_2}\gamma_2\right)A_1A_2\varepsilon^2 + \frac{12}{5}\frac{A_1}{B_2}\gamma_2A_2^3\varepsilon^3}{\frac{A_2}{A_1}\gamma_1 + \left[\frac{B_1}{A_1}(1-\gamma_1-\gamma_2) + 2\frac{A_1}{B_2}\gamma_2\right]A_2\varepsilon + 2\gamma_1A_1A_2\varepsilon^2 + 3\gamma_2\frac{A_1}{B_2}A_2^3\varepsilon^3}. \quad (4)$$

Here, we have neglected the phase shifts between outgoing  $l + 1$  and  $l - 1$  partial waves for simplicity.

To apply this model to the pyridinide anions, we must first determine an appropriate parameterization of the basis set defined by Eqs. (S3) and (S7). We fix  $Z_0$  and  $Z_1$  to the values presented above for the *para* isomer,  $Z_0 = Z_1 = 0.885$ . Based on the orbitals in Fig. 7, the *ortho* isomer is expected to show the most appreciable *d*-character, and so the experimental PAD for this isomer was fit to Eq. (4) to determine an appropriate value of  $Z_2$ . This gives parameter values of  $Z_2 = 1.45(8)$ ,  $\gamma_1 = 0.03(2)$ , and  $\gamma_2 = 0.68(13)$  for the *ortho* isomer. The extracted value of  $Z_2$  as well as the previously set value of  $Z_1$  gives Hanstorp coefficients of  $A_2 = 0.5$  and  $B_2 = 2.1 \text{ eV}^{-1}$ .

To treat the other two isomers, this value of  $Z_2 = 1.45$  is fixed, and the fractional *p*- and *d*-characters are extracted by fitting Eq. (4) to the experimental PAD for the *meta* and *para* isomers. The results of this mixed-*spd* treatment are shown as solid lines in Fig. 6, and the extracted fractional *s*, *p*, and *d* characters are presented in Table IV for all three isomers. These results agree well with the intuitive expectations given the appearance of the HOMOs in Fig. 7. The *p*-pyridinide isomer shows zero fractional *d*-character, as expected

for a PAD that is well-described by the mixed-*sp* model. The *m*-pyridinide isomer shows similar fractional character, with slightly more *s*-character and small nonzero *d*-character. The *o*-pyridinide isomer is roughly two-thirds *d*-character, with very little *p*-character. This trend suggests that, as the site of deprotonation moves toward the carbon atom, the fractional *d* character in the resultant anion HOMO increases. This is not a result of the involvement of atomic *d*-orbitals but rather due to the increased delocalization of the orbital resulting from the involvement of N-centered *p*-like orbitals, leading to a greater number of angular nodes which are associated with higher angular momenta.

### C. Bond-dissociation energies of pyridine and isomeric stabilities

Previously, the measured gas-phase acidity of the C<sub>4</sub> position of the pyridine ring  $\Delta H_{acid}^\circ(C_4) = 389.9 \pm 2.0 \text{ kcal mol}^{-1}$  was used in conjunction with the experimental electron affinity of the *p*-pyridyl radical to calculate the bond dissociation enthalpy of the C<sub>4</sub>H bond of pyridine,<sup>27</sup>

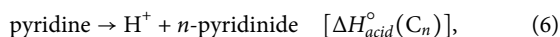
$$\text{BDE}(C_4H) = \Delta H_{acid}^\circ(C_4) + \text{EA}(C_4^\bullet) - \text{IE}(H), \quad (5)$$

where  $\text{IE}(H) = 313.6 \text{ kcal mol}^{-1}$  is the ionization energy of atomic hydrogen. The measurement of the EAs for the other two radical isomers motivates a similar calculation for the C<sub>3</sub>H and C<sub>2</sub>H BDEs. However, due to the relative stability of the *p*-pyridinide isomer, experimental measurements of  $\Delta H_{acid}^\circ(C_3)$  and  $\Delta H_{acid}^\circ(C_2)$  are not available. Thus, instead of using purely experimental results to calculate the *meta* and *ortho* analogs of Eq. (5), we employ a hybrid experimental-theoretical approach akin to that used previously to treat the oxazole<sup>29</sup> and furan<sup>32</sup> C-H bonds, as was discussed briefly in Sec. III.

**TABLE IV.** Fractional *s*, *p*, and *d*-characters of the detached orbital of each of the three pyridinide anion isomers as determined by application of the mixed-*spd* model to the experimental results. Uncertainties correspond to the standard error obtained from a least-squares fitting of the experimental data, and  $\gamma_0 = 1 - \gamma_1 - \gamma_2$ .

	$\gamma_0$	$\gamma_1$	$\gamma_2$
<i>para</i>	0.12	0.88(3)	0.00(4)
<i>meta</i>	0.22	0.71(5)	0.07(6)
<i>ortho</i>	0.30	0.03(2)	0.67(12)

The CBS-QB3 method is a chemically accurate procedure which can be used to calculate absolute enthalpies of molecular species. This was used to obtain the enthalpy change associated with heterolytic C–H bond cleavage, i.e., the gas-phase acidity,



for all three anion isomers. For each carbon position on the pyridine ring, we first find  $\delta_n$  [Eq. (2)], which expresses the difference in gas-phase acidities as compared to the 4-position for which an experimental value is already available. The CBS-QB3 enthalpies of the pyridinide anions for  $T = 298$  K (Table S6 of the supplementary material) give  $\delta_2 = 9.9$  and  $\delta_3 = 1.7$  kcal mol<sup>-1</sup>. Taking these differences to be accurate to within 2.0 kcal mol<sup>-1</sup>—the uncertainty on the experimental measurement of  $\Delta H_{\text{acid}}^{\circ}(\text{C}_4)$ —we then estimate the gas-phase acidity of the C<sub>2</sub> and C<sub>3</sub> positions of pyridine as

$$\Delta H_{\text{acid}}^{\circ}(\text{C}_n) = \delta_n + \Delta H_{\text{acid}}^{\circ}(\text{C}_4), \quad (7)$$

giving  $\Delta H_{\text{acid}}^{\circ}(\text{C}_3) = 391.6 \pm 2.0$  and  $\Delta H_{\text{acid}}^{\circ}(\text{C}_2) = 399.8 \pm 2.0$  kcal mol<sup>-1</sup>. Using the experimental EAs provided in Tables I–III as well as equations analogous to Eq. (5), we obtain enthalpies of BDE(C<sub>3</sub>H) = 111.4 ± 2.0 and BDE(C<sub>2</sub>H) = 106.2 ± 2.0 kcal mol<sup>-1</sup> for pyridine. The purely experimental value of BDE(C<sub>4</sub>H) calculated using the cryo-SEVI value for the EA of *p*-pyridyl is identical to that reported previously, 110.4 ± 2.0 kcal mol<sup>-1</sup>.

It should be noted that the measured EAs technically correspond to a temperature of 0 K and thus should be corrected in order to be used alongside the  $T = 298$  K quantities included in Eq. (5). The thermal correction, [ $H^{298}(\text{neutral}) - H^0(\text{neutral})$ ] – [ $H^{298}(\text{anion}) - H^0(\text{anion})$ ], may be calculated from our absolute enthalpies in Table S6 and is found to be < 0.2 kcal mol<sup>-1</sup> for all three isomers. As this is substantially smaller than the uncertainty in the experimental gas phase acidity of the C<sub>4</sub> position, we have neglected this correction here.

Table V presents the experimental-theoretical values for BDE(C<sub>*n*</sub>H) and  $\Delta H_{\text{acid}}^{\circ}(\text{C}_n)$ , the  $\delta_n$  values used in calculation of  $\Delta H_{\text{acid}}^{\circ}(\text{C}_n)$ , and the experimental EAs for the pyridyl radicals obtained from the cryo-SEVI spectra. These thermodynamic quantities reflect the relative energies of the anion and neutral isomers, which are provided in Fig. 1 for the B3LYP/6-311+G\* level of theory. For the neutral radicals, the *m*- and *p*-pyridyl isomers are within 2.5 kcal mol<sup>-1</sup> of each other, resulting in similar BDEs for the C<sub>3</sub> and C<sub>4</sub> positions of pyridine. The corresponding anion isomers are

**TABLE V.** Thermodynamic properties of the C<sub>*n*</sub> ring positions of pyridine ( $n = 2, 3, 4$ ) and the *x*-pyridyl radicals ( $x = p, m, o$ ). The gas phase acidity of the C<sub>4</sub> position of pyridine is obtained from previous measurements,<sup>27</sup> and values for the other two positions were obtained using the hybrid experimental-theoretical approach described in Sec. V C. BDEs are obtained for all carbon positions using Eq. (5).

<i>x</i>	<i>n</i>	EA( <i>x</i> -pyridyl)	$\Delta H_{\text{acid}}^{\circ}(\text{C}_n)$	BDE (C <sub><i>n</i></sub> H)
<i>p</i>	4	34.122 ± 0.012	389.9 ± 2.0	110.4 ± 2.0
<i>m</i>	3	33.375 ± 0.012	391.6 ± 2.0	111.4 ± 2.0
<i>o</i>	2	19.991 ± 0.016	399.8 ± 2.0	106.2 ± 2.0

similarly close in energy, resulting in similar gas-phase acidities for the *meta* and *para* carbons of pyridine. This similarity is consistent with the observation that both anion isomers are formed by deprotonation of pyridine by F<sup>-</sup> (Fig. S1). The small energy differences found in both charge states for these two isomers are the cause of the small difference in EAs (~30 meV) determined for the *p*- and *m*-pyridyl radicals.

The *ortho* isomer of both anion and neutral has energies which deviate more substantially from the other two isomers. The *o*-pyridyl radical is more stable than the other two isomers by 5 kcal mol<sup>-1</sup>, in agreement with the result that the C<sub>2</sub> position of pyridine has the weakest CH bond. The stabilization of the *o*-pyridyl radical has previously been suggested to be a consequence of two-center three-electron (2c, 3e) interactions between the unpaired electron and nitrogen lone pair for this radical isomer.<sup>17</sup> In contrast, the *o*-pyridinide anion is the highest-energy isomer for this charge state, lying several hundred millielectron volt above the other two anion isomers. This shift is attributed to destabilizing steric interactions resulting from repulsion of the C- and N-centered lone pairs. Thus, whereas the proximity between the site of deprotonation and the nitrogen lone pair results in stabilization of the neutral radical through (2c, 3e) bonding, the addition of an extra electron results in destabilization due to repulsion between the adjacent lone pairs. These effects are reflected in the low EA of *o*-pyridyl, a consequence of the simultaneous stabilization of the neutral and destabilization of the anion.

## VI. CONCLUSION

High-resolution photoelectron spectra have been obtained for all three pyridinide anions, yielding insight into the vibronic structure and energetics of the three pyridyl radicals. This work represents the first reported photoelectron spectra for the *m*- and *o*-pyridinide isomers and provides a substantial improvement in resolution over prior results for *p*-pyridinide. The resultant spectra are found to be in good agreement with Franck-Condon simulations based on B3LYP/6-311+G\* calculations, enabling extraction of a number of vibrational frequencies for each neutral isomer. In addition to resolving fine structure that would be obscured in a lower-resolution experiment, these results allow for observation of subtle vibrational effects such as anharmonic coupling between close-lying vibrational levels of the *p*-pyridyl radical.

The photoelectron angular distributions have been modeled using a three-component implementation of the generalized mixing model proposed by Sanov,<sup>42</sup> revealing chemically intuitive isomeric trends in the highest-occupied molecular orbitals of the pyridinide anions. Whereas the *p*-pyridinide PAD is found to be well-described by a HOMO consisting only of *s* and *p* components, the *o*-pyridinide PAD suggests substantially more *d*-character in the detached orbital. This analysis indicates that as the distance between the deprotonated carbon and the heteroatom is decreased, the angular momentum of the detached orbital is increased, which is related to the extent of delocalization of this MO. Finally, the measured electron affinities of each neutral radical were used with experimental and theoretical gas-phase acidities to obtain experimental-theoretical estimations of the CH bond dissociation enthalpies of pyridine, and these energies are related to the relative stabilities of the anion and neutral isomers.

## SUPPLEMENTARY MATERIAL

See [supplementary material](#) for Sections S1–S3, Figures S1–S6, and Tables S1–S9.

## ACKNOWLEDGMENTS

This research was funded by the Director, Office of Basic Energy Sciences, Chemical Sciences Division of the U.S. Department of Energy, under Contract No. DE-AC02-05CH11231. M.C.B. thanks the Department of Defense for a National Defense Science and Engineering Graduate Fellowship, and K.B. acknowledges a National Science Foundation Graduate Research Fellowship. The authors acknowledge NIH Grant No. S10OD023532 for funding the computational facilities used for the current results.

## REFERENCES

- J. R. Kershaw, *Fuel* **62**, 1430 (1983).
- S. Wallace, K. D. Bartle, and D. L. Perry, *Fuel* **68**, 1450 (1989).
- K. L. Smith, L. D. Smoot, T. H. Fletcher, and R. J. Pugmire, *The Structure and Reaction Processes of Coal*, The Plenum Chemical Engineering Series (Springer, 1994), Vol. 4.
- L. E. Fried, M. R. Manaa, P. F. Pagoria, and R. L. Simpson, *Annu. Rev. Mater. Res.* **31**, 291 (2001).
- B. J. Finlayson-Pitts and J. N. Pitts, *Science* **276**, 1045 (1997).
- A. E. Axworthy, V. H. Dayan, and G. B. Martin, *Fuel* **57**, 29 (1978).
- Z.-C. Wang, C. A. Cole, N. J. Demarais, T. P. Snow, and V. M. Bierbaum, *J. Am. Chem. Soc.* **137**, 10700 (2015).
- J. C. Loison, E. Hebrard, M. Dobrijevic, K. M. Hickson, F. Daralp, V. Hue, G. Gronoff, O. Venot, and Y. Benilan, *Icarus* **247**, 218 (2015).
- T. J. Houser, M. E. McCarville, and T. Biftu, *Int. J. Chem. Kinet.* **12**, 555 (1980).
- J. Jones, G. B. Bacskay, J. C. Mackie, and A. Doughty, *J. Chem. Soc. Faraday Trans.* **91**, 1587 (1995).
- J. H. Kiefer, Q. Zhang, R. D. Kern, J. Yao, and B. Jursic, *J. Phys. Chem. A* **101**, 7061 (1997).
- N. R. Hore and D. K. Russell, *J. Chem. Soc., Perkin Trans. 2*, 269 (1998).
- R. Liu, T. T.-S. Huang, J. Tittle, and D. Xia, *J. Phys. Chem. A* **104**, 8368 (2000).
- X. Cheng, L. Niu, Y. Zhao, and Z. Zhou, *Spectrochim. Acta A* **60**, 907 (2004).
- X. L. Cheng, Y. Y. Zhao, and Z. Y. Zhou, *J. Mol. Struct.: THEOCHEM* **678**, 17 (2004).
- X. Cheng, *J. Mol. Struct.: THEOCHEM* **731**, 89 (2005).
- C. Sah, L. Jacob, M. Saraswat, and S. Venkataramani, *J. Phys. Chem. A* **121**, 3781 (2017).
- M. Lucas, J. Minor, J. Zhang, and C. Brazier, *J. Phys. Chem. A* **117**, 12138 (2013).
- M. Lucas, J. Minor, J. Zhang, and C. Brazier, *Chin. J. Chem. Phys.* **27**, 621 (2014).
- A. Korte, A. Mardyukov, and W. Sander, *Aust. J. Chem.* **67**, 1324 (2014).
- P. H. Kasai and D. McLeod, *J. Am. Chem. Soc.* **92**, 6085 (1970).
- J. E. Bennett and B. Mile, *J. Phys. Chem.* **75**, 3432 (1971).
- P. H. Kasai and D. McLeod, *J. Am. Chem. Soc.* **94**, 720 (1972).
- H. Zemel and R. W. Fessenden, *J. Phys. Chem.* **79**, 1419 (1975).
- P. G. Wenthold and W. C. Lineberger, *Acc. Chem. Res.* **32**, 597 (1999).
- A. Sanov, *Annu. Rev. Phys. Chem.* **65**, 341 (2014).
- S. W. Wren, K. M. Vogelhuber, J. M. Garver, S. Kato, L. Sheps, V. M. Bierbaum, and W. C. Lineberger, *J. Am. Chem. Soc.* **134**, 6584 (2012).
- L. M. Culberson, C. C. Blackstone, and A. Sanov, *J. Phys. Chem. A* **117**, 11760 (2013).
- L. M. Culberson, C. C. Blackstone, A. A. Wallace, and A. Sanov, *J. Phys. Chem. A* **119**, 9770 (2015).
- B. S. Schafman and P. G. Wenthold, *J. Org. Chem.* **72**, 1645 (2007).
- E. R. Grumblin and A. Sanov, *J. Chem. Phys.* **135**, 164302 (2011).
- J. A. DeVine, M. L. Weichman, S. J. Lyle, and D. M. Neumark, *J. Mol. Spectrosc.* **332**, 16 (2017).
- A. M. Oliveira, Y. J. Lu, J. H. Lehman, P. B. Changala, J. H. Baraban, J. F. Stanton, and W. C. Lineberger, *J. Am. Chem. Soc.* **137**, 12939 (2015).
- A. Osterwalder, M. J. Nee, J. Zhou, and D. M. Neumark, *J. Chem. Phys.* **121**, 6317 (2004).
- D. M. Neumark, *J. Phys. Chem. A* **112**, 13287 (2008).
- C. Hock, J. B. Kim, M. L. Weichman, T. I. Yacovitch, and D. M. Neumark, *J. Chem. Phys.* **137**, 244201 (2012).
- M. L. Weichman and D. M. Neumark, *Annu. Rev. Phys. Chem.* **69**, 101 (2018).
- J. B. Kim, M. L. Weichman, T. I. Yacovitch, C. Shih, and D. M. Neumark, *J. Chem. Phys.* **139**, 104301 (2013).
- M. L. Weichman, J. B. Kim, and D. M. Neumark, *J. Phys. Chem. A* **119**, 6140 (2015).
- M. L. Weichman, J. B. Kim, J. A. DeVine, D. S. Levine, and D. M. Neumark, *J. Am. Chem. Soc.* **137**, 1420 (2015).
- M. L. Weichman, J. A. DeVine, D. S. Levine, J. B. Kim, and D. M. Neumark, *Proc. Natl. Acad. Sci. U. S. A.* **113**, 1698 (2016).
- D. Khuseynov, C. C. Blackstone, L. M. Culberson, and A. Sanov, *J. Chem. Phys.* **141**, 124312 (2014).
- U. Even, J. Jortner, D. Noy, N. Lavie, and C. Cossart-Magos, *J. Chem. Phys.* **112**, 8068 (2000).
- C. H. Depuy, V. M. Bierbaum, L. A. Flippin, J. J. Grabowski, G. K. King, R. J. Schmitt, and S. A. Sullivan, *J. Am. Chem. Soc.* **102**, 5012 (1980).
- C. H. Depuy, S. R. Kass, and G. P. Bean, *J. Org. Chem.* **53**, 4427 (1988).
- W. C. Wiley and I. H. McLaren, *Rev. Sci. Instrum.* **26**, 1150 (1955).
- A. T. J. B. Eppink and D. H. Parker, *Rev. Sci. Instrum.* **68**, 3477 (1997).
- J. A. DeVine, A. A. Taka, M. C. Babin, M. L. Weichman, H. P. Hratchian, and D. M. Neumark, *J. Chem. Phys.* **148**, 222810 (2018).
- D. W. Chandler and P. L. Houston, *J. Chem. Phys.* **87**, 1445 (1987).
- M. B. Doyle, C. Abeyasera, and A. G. Suits, NuACQ, <https://chemistry.missouri.edu/people/suits>.
- B. D. Phys, *Chem. Chem. Phys.* **16**, 570 (2014).
- M. Scheer, C. A. Brodie, R. C. Bilodeau, and H. K. Haugen, *Phys. Rev. A* **58**, 2051 (1998).
- C. Blondel, W. Chaibi, C. Delsart, C. Drag, F. Goldfarb, and S. Kroger, *Eur. Phys. J. D* **33**, 335 (2005).
- J. Cooper and R. N. Zare, *J. Chem. Phys.* **48**, 942 (1968).
- Y. H. Shao, Z. T. Gan, E. Epifanovsky, A. T. B. Gilbert, M. Wormit, J. Kussmann, A. W. Lange, A. Behn, J. Deng, X. T. Feng, D. Ghosh, M. Goldey, P. R. Horn, L. D. Jacobson, I. Kaliman, R. Z. Khaliullin, T. Kus, A. Landau, J. Liu, E. I. Proynov, Y. M. Rhee, R. M. Richard, M. A. Rohrdanz, R. P. Steele, E. J. Sundstrom, H. L. Woodcock, P. M. Zimmerman, D. Zuev, B. Albrecht, E. Alguire, B. Austin, G. J. O. Beran, Y. A. Bernard, E. Berquist, K. Brandhorst, K. B. Bravaya, S. T. Brown, D. Casanova, C. M. Chang, Y. Q. Chen, S. H. Chien, K. D. Closser, D. L. Crittenden, M. Diedenhofen, R. A. DiStasio, H. Do, A. D. Dutoi, R. G. Edgar, S. Fatehi, L. Fusti-Molnar, A. Ghysels, A. Golubeva-Zadorozhnyaya, J. Gomes, M. W. D. Hanson-Heine, P. H. P. Harbach, A. W. Hauser, E. G. Hohenstein, Z. C. Holden, T. C. Jagau, H. J. Ji, B. Kaduk, K. Khistyayev, J. Kim, J. Kim, R. A. King, P. Klunzinger, D. Kosenkov, T. Kowalczyk, C. M. Krauter, K. U. Lao, A. D. Laurent, K. V. Lawler, S. V. Levchenko, C. Y. Lin, F. Liu, E. Livshits, R. C. Lochan, A. Luenser, P. Manohar, S. F. Manzer, S. P. Mao, N. Mardirossian, A. V. Marenich, S. A. Maurer, N. J. Mayhall, E. Neuscamman, C. M. Oana, R. Olivares-Amaya, D. P. O'Neill, J. A. Parkhill, T. M. Perrine, R. Peverati, A. Prociuk, D. R. Rehn, E. Rosta, N. J. Russ, S. M. Sharada, S. Sharma, D. W. Small, A. Sodt, T. Stein, D. Stuck, Y. C. Su, A. J. W. Thom, T. Tsuchimochi, V. Vanovschi, L. Vogt, O. Vydrov, T. Wang, M. A. Watson, J. Wenzel, A. White, C. F. Williams, J. Yang, S. Yeganeh, S. R. Yost, Z. Q. You, I. Y. Zhang, X. Zhang, Y. Zhao, B. R. Brooks, G. K. L. Chan, D. M. Chipman, C. J. Cramer, W. A. Goddard, M. S. Gordon, W. J. Hehre, A. Klamt, H. F. Schaefer, M. W. Schmidt, C. D. Sherrill, D. G. Truhlar, A. Warshel, X. Xu, A. Aspuru-Guzik, R. Baer, A. T. Bell, N. A. Besley, J. D. Chai, A. Dreuw, B. D. Dunietz, T. R. Furlani, S. R. Gwaltney, C. P. Hsu, Y. S. Jung, J. Kong, D. S. Lambrecht, W. Z. Liang, C. Ochsenfeld, V. A. Rassolov, L. V. Slipchenko, J. E. Subotnik, V. T. Van, J. M. Herbert, A. I. Krylov, P. M. W. Gill, and M. Head-Gordon, *Mol. Phys.* **113**, 184 (2015).
- V. A. Mozhaykiy and A. Krylov, ezSpectrum 3.0, <http://iopshell.usc.edu/downloads/>.

- <sup>57</sup>M. J. Frisch, G. W. Trucks, H. B. Schlegel, G. E. Scuseria, M. A. Robb, J. R. Cheeseman, G. Scalmani, V. Barone, G. A. Petersson, H. Nakatsuji, X. Li, M. Caricato, A. V. Marenich, J. Bloino, B. G. Janesko, R. Gomperts, B. Mennucci, H. P. Hratchian, J. V. Ortiz, A. F. Izmaylov, J. L. Sonnenberg, D. Williams-Young, F. Ding, F. Lipparini, F. Egidi, J. Goings, B. Peng, A. Petrone, T. Henderson, D. Ranasinghe, V. G. Zakrzewski, J. Gao, N. Rega, G. Zheng, W. Liang, M. Hada, M. Ehara, K. Toyota, R. Fukuda, J. Hasegawa, M. Ishida, T. Nakajima, Y. Honda, O. Kitao, H. Nakai, T. Vreven, K. Throssell, J. A. Montgomery, Jr., J. E. Peralta, F. Ogliaro, M. J. Bearpark, J. J. Heyd, E. N. Brothers, K. N. Kudin, V. N. Staroverov, T. A. Keith, R. Kobayashi, J. Normand, K. Raghavachari, A. P. Rendell, J. C. Burant, S. S. Iyengar, J. Tomasi, M. Cossi, J. M. Millam, M. Klene, C. Adamo, R. Cammi, J. W. Ochterski, R. L. Martin, K. Morokuma, O. Farkas, J. B. Foresman, and D. J. Fox, *GAUSSIAN 16*, Revision B.01, Gaussian, Inc., Wallingford, CT, 2016.
- <sup>58</sup>J. A. Montgomery, M. J. Frisch, and J. W. Ochterski, *J. Chem. Phys.* **112**, 6532 (2000).
- <sup>59</sup>G. P. F. Wood and L. Radom, *J. Chem. Phys.* **125**, 094106 (2006).
- <sup>60</sup>E. P. Wigner, *Phys. Rev.* **73**, 1002 (1948).
- <sup>61</sup>D. Hanstorp, C. Bengtsson, and D. J. Larson, *Phys. Rev. A* **40**, 670 (1989).
- <sup>62</sup>J. L. Hall and M. W. Siegel, *J. Chem. Phys.* **48**, 943 (1968).
- <sup>63</sup>A. Sanov, E. R. Grumblin, D. J. Goebbert, and L. M. Culberson, *J. Chem. Phys.* **138**, 054311 (2013).